Research Square

Preprints are preliminary reports that have not undergone peer review.
They should not be considered conclusive, used to inform clinical practice,
or referenced by the media as validated information.

Fixed laboratory-axis readout of retained qubit information near a Floquet crossing

Matthias Jakob

mathias.jakob@kbw-gruppe.de

Kolping-Schulen Neckarpark

Research Article

Keywords: Floquet dynamics, open quantum systems, quantum Fisher information, fixed-axis measurement, hierarchical equations of motion

Posted Date: November 23rd, 2026

DOI: https://doi.org/10.21203/rs.3.rs-11672245/v1

License: This work is licensed under a Creative Commons Attribution 4.0 International License.
Read Full License

Additional Declarations: No competing interests reported.

Fixed laboratory-axis readout of retained qubit information near a Floquet crossing

Matthias Jakob

Kolping-Schulen Neckarpark, Lenore-Volz-Strasse 1,
70372 Stuttgart, Germany
mathias.jakob@kbw-gruppe.de

8 November 2026

Abstract

Periodic driving can retain initial-state information, but its usefulness depends on the permitted readout. We study local estimation of an initial-state mixture coefficient in a driven spin–boson model. Each independently prepared copy is measured once at a uniformly sampled, recorded delay using one unchanged Pauli axis. Hierarchical equations of motion yield approximately twice the laboratory-x Fisher information at a Floquet-crossing reference as at two spectrum-selected controls. This readout accesses 90.81% of the mean quantum Fisher information and is nearly optimal within constant binary Pauli projections. The reference-to-control advantage persists throughout a 15° input cone within reconstructed numerical maps, but reverses for a known y input. A broader amplitude scan places the reference close to the largest sampled information. Together, these results give a reproducible, input-dependent benchmark that distinguishes information retained in the state from information accessible to a fixed laboratory readout.

Keywords: Floquet dynamics; open quantum systems; quantum Fisher information; fixed-axis measurement; hierarchical equations of motion.

1 Introduction

Periodic control can help a qubit retain an initial-state contrast, but that contrast must remain accessible to the measurement available at readout. A fixed laboratory observable is a particularly simple constraint: its axis is unchanged even when the measurement delay is known. We ask how much information this measurement can recover from a driven, dissipative qubit. The task concerns delayed access to initially encoded information; it does not seek an advantage over immediate readout.

Retained information denotes the mean quantum Fisher information (QFI) for the initial-state coefficient. Accessible information denotes the classical Fisher information supplied by the specified measurement; the accessible fraction is this value divided by the retained information. All three refer to local parameter estimation under the same distribution of recorded delays.

Floquet theory describes periodic dynamics through quasienergies and micromotion [1, 2]. Its interplay with dissipation is treated in established and modern reviews [3, 4], and longer coherence times have been demonstrated in driven fluxonium [5]. For the driven spin–boson model used here, Follia, Vacchini, and Breuer found enhanced relaxation times and memory effects near quasienergy crossings using hierarchical equations of motion (HEOM), and identified x-oriented antipodal states as favorable for trace-distance backflow [6]. Their subsequent preprint develops a second-order Floquet time-convolutionless description [7]. Here we quantify how much classical Fisher information one unchanged laboratory Pauli axis supplies when each independently prepared copy has a recorded readout delay. This measurement-constrained estimation task separates the retained amount from the share accessible to a constant axis.

Physical routes to Floquet-qubit readout include adiabatic mapping [8], engineered longitudinal detection [9], and fluorescence measurement [10]. The construction of Gandon et al. already uses a laboratory-σ_x coupling to a readout mode [9]. Our contribution is a quantitative benchmark for ideal terminal projections, rather than a new use of this Pauli component or a comparison of hardware fidelity.

QFI supplies the locally optimal measurement benchmark [11, 12]. Its attainability depends on the allowed measurements and statistical task [13]; measurement restrictions also generate hierarchies for composite systems [14]. Bloch-vector formulas make initially encoded qubit parameters accessible to numerical analysis under dissipation [15]. We distinguish this information from trace-distance backflow [16] and QFI flow [17]. The unknown parameter is a coefficient of the initial density operator, while the drive and bath are known. This differs from Floquet sensing of Hamiltonian parameters [18, 19], including the Ising coupling and transverse field studied by Ullah et al. [20]. Manya, Tsypilnikov and Iemini study feasible near-optimal observables for AC-field sensing in a recent preprint [21]. Our unknown belongs to the initial state, and one Pauli axis must serve an entire distribution of recorded delays.

We use HEOM to compare a crossing reference with two controls selected from the isolated Floquet spectrum before their dissipative calculations. With unchanged encoding and laboratory axes, the reference supplies about twice the laboratory-x information of either control. Direct axis optimization and an algebraic envelope show how little can be gained within the constant-axis class. Local bath variations, known input directions and a broader amplitude scan then test the extent of this advantage. The input study establishes a favorable neighborhood and an explicit counterexample. Preliminary time-convolutionless calculations enter only through the inherited calibration; all principal dynamical results use HEOM.

2 Dynamics and statistical protocol

2.1 Driven qubit and bath

With $\hbar = k_{\mathrm{B}} = 1$, the Hamiltonian is

$$H(t) = H_S(t) + H_B + H_I, \qquad H_S(t) = \frac{\omega_0}{2}\sigma_z + \Omega\cos(\omega t)\sigma_x, \tag{1}$$

$$H_B = \sum_k \nu_k a_k^\dagger a_k, \qquad H_I = \sigma_x \otimes B, \qquad B = \sum_k g_k(a_k + a_k^\dagger). \tag{2}$$

Here σ_j are Pauli matrices and a_k annihilates a bath mode. The bath has zero mean and a Lorentz–Drude spectral density [22, 23], with the explicit normalization

$$J_B(\nu) = \alpha\Lambda \frac{\nu}{\nu^2 + \Lambda^2}, \tag{3}$$

$$C_B(u) = \frac{1}{2\pi} \int_0^\infty J_B(\nu) \left[\coth\!\left(\frac{\nu}{2T_B}\right) \cos(\nu u) - i \sin(\nu u) \right] d\nu. \tag{4}$$

The bath temperature is T_B, and α and Λ have frequency units. Frequencies are reported in units of ω_0 and times in ω_0^{-1}. We set $\omega = \omega_0 = 1$, with reference values $(\alpha, \Lambda, T_B) = (0.1, 1.2, 1)$. The drive phase is known and fixed.

Every repetition starts in $\rho_\theta(0) \otimes e^{-H_B/T_B}/Z_B$. We use the HEOM approach [22], implemented in QuTiP 5.3.1 [24, 25], with no secular or rotating-wave reduction of Eq. (1). Matching Eq. (4) to the QuTiP Drude convention requires $\lambda = \alpha/4$, $\gamma = \Lambda$, and temperature T_B. Initial non-root auxiliary density operators are zero. Numerical settings and their refinements are given in the Supplementary Information (SI; Online Resource 1, `ESM1.pdf`).

2.2 Encoding, axes, and recorded times

The encoded family and its prescribed unit direction are

$$\rho_\theta(0) = \frac{I + \theta \boldsymbol{v} \cdot \boldsymbol{\sigma}}{2}, \qquad |\theta| \le 1, \tag{5}$$

$$\boldsymbol{v} = \boldsymbol{v}_0 \simeq (0.94443754, -0.07970011, -0.31888184). \tag{6}$$

The full-precision vectors are specified in the SI and the data files. All information quantities are evaluated locally at $\theta = 0$. This direction was inherited from a preliminary finite-horizon backflow search within a second-order time-convolutionless approximation [23]. The backflow objective follows the trace-distance approach of Breuer, Laine and Piilo [16]. Here it is a fixed, archived benchmark input, not an HEOM-optimized direction or a claim of global preparation optimality.

We propagate the physical endpoints $\rho_\pm(0) = (I \pm \boldsymbol{v} \cdot \boldsymbol{\sigma})/2$ separately. Linearity gives

$$\boldsymbol{r}_\theta(t) = \boldsymbol{b}(t) + \theta \boldsymbol{w}(t), \qquad \boldsymbol{b} = \frac{\boldsymbol{r}_+ + \boldsymbol{r}_-}{2}, \qquad \boldsymbol{w} = \frac{\boldsymbol{r}_+ - \boldsymbol{r}_-}{2}, \tag{7}$$

where $\boldsymbol{r}_\pm$ are laboratory Bloch vectors. The two constant measurement axes are

$$\begin{aligned} \boldsymbol{n}_x &= (1, 0, 0), \\ \boldsymbol{n}_* &\simeq (0.99996434, 0.00842767, -0.00053994). \end{aligned} \tag{8}$$

The secondary axis was also calibrated in the preliminary calculation. It lies 0.483866° from laboratory-x. Both prescribed axes and $\boldsymbol{v}_0$ remain unchanged throughout the primary drive and bath comparisons. The supplementary input study explicitly changes the known encoding direction. Separate numerical measurement optimizations are diagnostic and do not replace the fixed laboratory-x results. Table S1 in the SI distinguishes these roles and their provenance.

Each independently prepared copy is measured once at a time drawn uniformly from $[0, T]$. The time is recorded together with the binary outcome $s = \pm 1$. Its label allows an outcome to be interpreted using the response at that delay. If the label is discarded, responses at different times are mixed before inference and information can be lost. Thus the delay is known for

every outcome, while the laboratory axis stays fixed across the entire delay distribution. For a unit axis $\boldsymbol{n}$, the joint likelihood is

$$p_\theta(s,t) = \frac{1}{T}\frac{1 + s\boldsymbol{n}^\mathsf{T}[\boldsymbol{b}(t) + \theta\boldsymbol{w}(t)]}{2}. \tag{9}$$

Since the sampling density does not depend on θ, the classical Fisher information per copy is

$$\mathcal{J}(\boldsymbol{n}) = \langle j_{\boldsymbol{n}}\rangle_T\,, \qquad j_{\boldsymbol{n}}(t) = \frac{[\boldsymbol{n}^\mathsf{T}\boldsymbol{w}(t)]^2}{1 - [\boldsymbol{n}^\mathsf{T}\boldsymbol{b}(t)]^2}, \qquad \langle f\rangle_T = \frac{1}{T}\int_0^T f(t)\,dt. \tag{10}$$

All evaluated denominators are positive. For N independent copies, the joint information is $N\mathcal{J}$ and the local Cramér–Rao bound is $\mathrm{Var}_0(\hat{\theta}) \geq 1/(N\mathcal{J})$ for locally unbiased estimators under the usual regularity assumptions [12]. At $N = 10^4$, the reference and the left and right controls give standard-deviation lower bounds of approximately 0.01755, 0.02571, and 0.02447, respectively. These are local precision bounds, not demonstrated finite-sample estimator errors.

For sequential independent copies, the mean free-evolution time is $T/2$. If each copy also costs a known, parameter-independent time t_{oh} for preparation, measurement and reset, its long-run information rate is $\mathcal{J}/(T/2 + t_{\mathrm{oh}})$. The reported operating-point ratios are unchanged when T and this overhead are common. We do not optimize the delay distribution or make a hardware-specific throughput claim.

2.3 Quantum benchmark and constant-axis envelope

Using the symmetric logarithmic derivative (SLD), the qubit QFI of Eq. (7) is [11, 12, 15]

$$F_Q(t) = \|\boldsymbol{w}(t)\|^2 + \frac{[\boldsymbol{b}(t)^\mathsf{T}\boldsymbol{w}(t)]^2}{1 - \|\boldsymbol{b}(t)\|^2}, \qquad \overline{F_Q} = \langle F_Q\rangle_T. \tag{11}$$

This quantum reference uses the same recorded times and permits a locally optimal measurement chosen for each delay. It therefore allows more measurement control than any single constant axis. Define $\mathcal{J}_x = \mathcal{J}(\boldsymbol{n}_x)$, $\mathcal{J}_* = \mathcal{J}(\boldsymbol{n}_*)$, and

$$\eta_x = \mathcal{J}_x/\overline{F_Q}, \qquad \eta_* = \mathcal{J}_*/\overline{F_Q}. \tag{12}$$

The absolute information $\mathcal{J}_x$ and its accessible fraction η_x answer different questions.

For the class of constant binary Pauli projections, define

$$G = \langle \boldsymbol{w}\boldsymbol{w}^\mathsf{T}\rangle_T, \qquad H = \left\langle \frac{\boldsymbol{w}\boldsymbol{w}^\mathsf{T}}{1 - \|\boldsymbol{b}\|^2}\right\rangle_T. \tag{13}$$

The inequalities $0 \leq (\boldsymbol{n}^\mathsf{T}\boldsymbol{b})^2 \leq \|\boldsymbol{b}\|^2$ imply

$$\boldsymbol{n}^\mathsf{T}G\boldsymbol{n} \leq \mathcal{J}(\boldsymbol{n}) \leq \boldsymbol{n}^\mathsf{T}H\boldsymbol{n}, \qquad \max_{\|\boldsymbol{n}\|=1}\mathcal{J}(\boldsymbol{n}) \leq U \equiv \min\{\lambda_{\max}(H), \overline{F_Q}\}. \tag{14}$$

Consequently, $100(U - \mathcal{J}_x)/\overline{F_Q}$ bounds the possible improvement of another constant axis in percentage points. This is an elementary algebraic envelope, evaluated on the computed trajectories. It is not an interval-arithmetic bound on the continuum dynamics. For a unital trajectory, $\boldsymbol{b} = 0$ and the optimization reduces exactly to the largest eigenvalue of G.

The geometric reason for a fixed-axis loss is simple. At each delay the SLD selects a locally optimal direction. One constant axis can attain the mean QFI only if it is optimal at almost every informative delay. The SI gives the exact nonnegative quadratic loss and its controlled near-unital approximation, derived from the standard qubit formulas.

3 HEOM results

3.1 Controls selected from the Floquet spectrum

Exact quasienergy crossings in driven two-level systems can be associated with Floquet symmetries [26]. Here the comparison uses numerically resolved gaps and does not rely on a symmetry classification. We retain the archived crossing reference $\Omega_c = 9.001856389545972$. For the isolated propagator over one period $\tau = 2\pi/\omega$, quasienergies ϵ_j are defined by the eigenvalues $e^{-i\epsilon_j\tau}$. We use the reduced gap

$$\Delta_F(\Omega) = \min_{m\in\mathbb{Z}} |\epsilon_1(\Omega) - \epsilon_2(\Omega) + m\omega|. \tag{15}$$

At the predefined horizon $T = 150$, we choose the nearest root of $T\Delta_F = 2\pi$ on each side of Ω_c, along the first increasing sampled branch. The scan spacing is 0.0025, followed by root refinement. Both controls and the numerical acceptance criteria were saved before their HEOM propagations. No dissipative information value enters their selection.

The resulting controls are

$$\Omega_- = 8.887487160959518, \qquad \Omega_+ = 9.117649351028664. \tag{16}$$

Their distances from the reference are about 1.27% and 1.29%. Both gaps are $2\pi/150 = 0.04188790205$ within the recorded integration accuracy. The archived reference has a small residual gap 1.50×10^{-7}, corresponding to only 2.25×10^{-5} rad over the window. It is therefore treated as a crossing reference rather than retuned after the comparison. The selection separates one relative quasienergy phase cycle on the observation window; it does not match every dissipative timescale.

Table 1 Information per copy for uniformly sampled, recorded times in $[0, 150]$, locally at $\theta = 0$. Encoding, bath, phase and both constant binary Pauli projections are unchanged. $\overline{F_Q}$ is the time-adaptive quantum reference. The final column is $100(U - \mathcal{J}_x)/\overline{F_Q}$ in percentage points.

Point	Ω	$\overline{F_Q}$	$\mathcal{J}_x$	$\mathcal{J}_*$	$100\eta_x$	upper gap
Left	8.887487	0.179641	0.151229	0.151269	84.1838	0.07932
Reference	9.001856	0.357351	0.324502	0.324526	90.8075	0.03179
Right	9.117649	0.195672	0.166950	0.166989	85.3213	0.07533

Figure 1 and Table 1 show that the crossing reference approximately doubles the available laboratory-x information: the factors relative to the left and right controls are 2.14577 and 1.94371. Its advantage factors as

$$\frac{\mathcal{J}_x^{\mathrm{ref}}}{\mathcal{J}_x^{\mathrm{ctrl}}} = \frac{\overline{F_Q}^{\mathrm{ref}}}{\overline{F_Q}^{\mathrm{ctrl}}} \frac{\eta_x^{\mathrm{ref}}}{\eta_x^{\mathrm{ctrl}}}. \tag{17}$$

The retained mean QFI increases by factors of about 1.99 and 1.83, whereas the accessible share increases by only about 8% and 6%. Most of the information advantage therefore comes from better retention, with a smaller contribution from measurement accessibility.

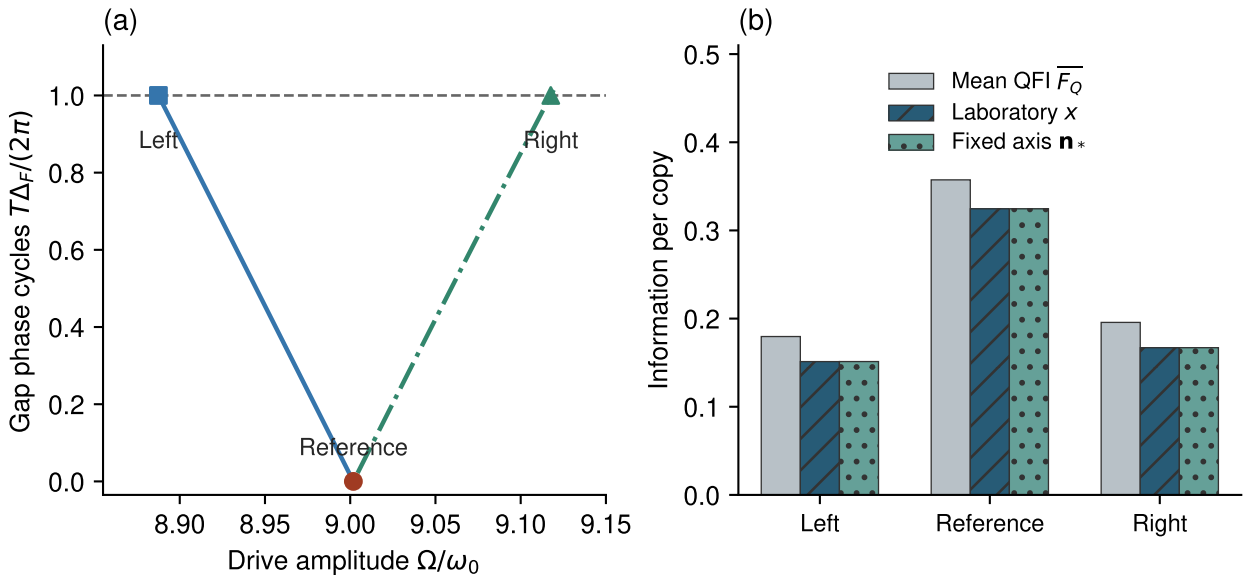

Fig. 1 Spectrum-selected controls and their information at $T = 150$. (a) Reduced-gap phase cycles, with the selection level shown dashed. Lines connect the computed spectral samples. (b) Mean QFI and information of the two unchanged constant axes. The two classical values nearly coincide; their small difference is resolved in Table 1

3.2 Direct optimization within constant Pauli projections

We also maximize Eq. (10) numerically on the unit sphere, using a direction grid, multiple constrained local searches [27] and an independent differential-evolution search [28], implemented with SciPy [29]. Define $\mathcal{J}_{\mathrm{num}} = \mathcal{J}(\boldsymbol{n}_{\mathrm{num}})$ for the best feasible axis found. It obeys $\mathcal{J}_x \le \mathcal{J}_{\mathrm{num}} \le \mathcal{J}_{\max}^{\mathrm{const}} \le U$, where $\mathcal{J}_{\max}^{\mathrm{const}}$ denotes the exact maximum on the evaluated trajectory. The numerical search and the algebraic upper bound are complementary checks.

Table 2 separates the gain available by changing a constant axis from the larger gain allowed by time-dependent optimal measurements. At the reference, laboratory-x obtains 99.99249% of $\mathcal{J}_{\mathrm{num}}$, while $\mathcal{J}_{\mathrm{num}}$ itself is only about 90.81% of $\overline{F_Q}$. Across all thirteen primary points, $\mathcal{J}_x/\mathcal{J}_{\mathrm{num}} > 99.95\%$, and the independently evaluated envelope limits any constant-axis improvement to less than 0.080 percentage points of mean QFI. The first statement compares feasible numerical axes; the second bounds the unsearched remainder on the computed trajectories. The SI gives every optimized axis and upper-bound gap. These optimizations diagnose the fixed-axis restriction; the prescribed input and the two reported laboratory axes remain unchanged.

Table 2 Numerical constant-axis optimization at $T = 150$, locally at $\theta = 0$. The last column is the angle between $\boldsymbol{n}_{\mathrm{num}}$ and laboratory-x in degrees. Percentages distinguish constant-axis performance from the time-adaptive quantum reference.

Point	$\mathcal{J}_{\mathrm{num}}$	$100\mathcal{J}_x/\mathcal{J}_{\mathrm{num}}$	$100\mathcal{J}_{\mathrm{num}}/\overline{F_Q}$	$100\eta_x$	angle
Left	0.15129248	99.95795	84.21924	84.18383	1.22751
Reference	0.32452615	99.99249	90.81429	90.80747	0.50845
Right	0.16700820	99.96509	85.35109	85.32130	1.11773

3.3 Dependence on the observation window

Figure 2 shows the same trajectories evaluated over shorter windows. The reference exceeds both controls at each reported horizon $T = 30, 60, 90, 120, 150$, with the ratios increasing from 1.2808 and 1.1788 at $T = 30$ to their values above at $T = 150$. The horizon 150 remains the predefined primary comparison.

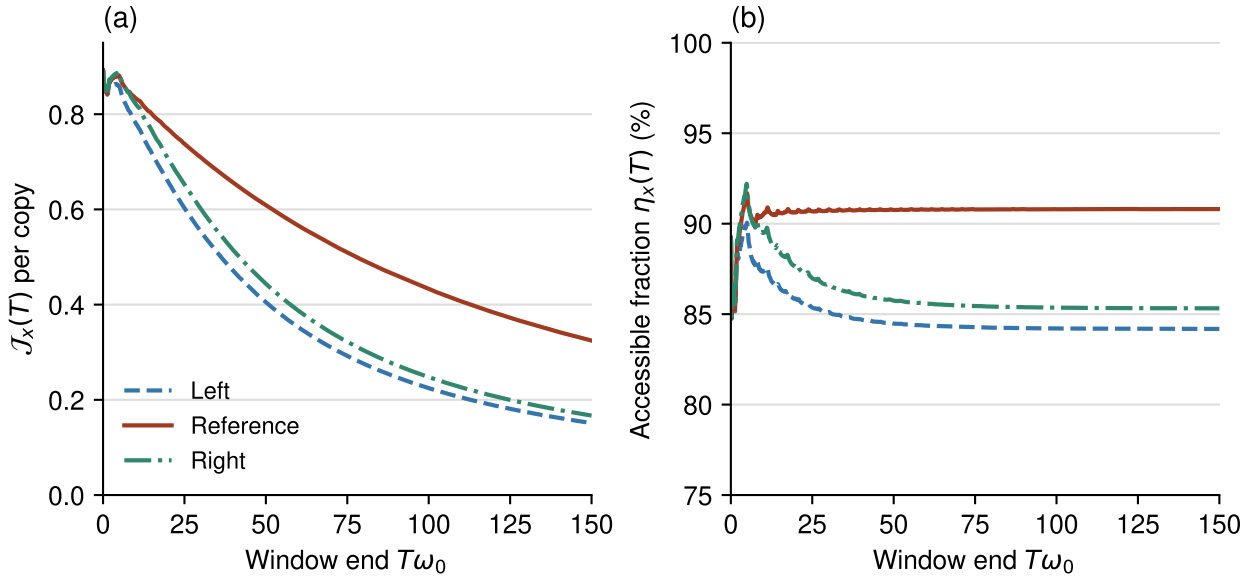

Fig. 2 Cumulative information from the three primary trajectories. (a) Laboratory-x information per copy. (b) Its fraction of mean QFI; the vertical scale is enlarged. Every point on a curve averages from zero to the displayed horizon. These curves do not represent additional propagations or a reselected time window

Instantaneous final-time information is distinct from the uniform-time protocol. At $t = 150$, the QFI is 0.0754123 at the reference and 0.00149525, 0.00182840 at the controls. The corresponding instantaneous laboratory-x information is 0.0701666, 0.00120887, and 0.00154014. This time is not an integer number of drive periods; micromotion contributes to these endpoint values. They are included as diagnostics, not substituted for the mean information.

3.4 Local drive and bath checks

The separate robustness batch contains eleven operating points. Five have drive offsets $\delta = \Omega - \Omega_c \in \{-0.001, -0.0005, 0, 0.0005, 0.001\}$ at the reference bath. Six vary one bath parameter at a time at Ω_c: $\alpha = 0.08, 0.12$, $\Lambda = 0.96, 1.44$, or $T_B = 0.8, 1.2$. All other quantities remain fixed.

Across these eleven points, $\mathcal{J}_x$ ranges from 0.275684 to 0.388063 and η_x from 90.5504% to 90.9943%. The constant-axis upper gap is at most 0.0456 percentage points. Figure 3 shows why the absolute and relative quantities should be reported together: changes in the retained amount can be appreciable while the accessible fraction stays close to 91%. The Supplementary Information lists every point.

The small drive offsets are about a hundred times narrower than those in Eq. (16). They test local stability; a broader amplitude study below quantifies performance widths. The bath cases are separately known settings, not a simultaneous uncertainty box or an estimator robust to unknown nuisance parameters.

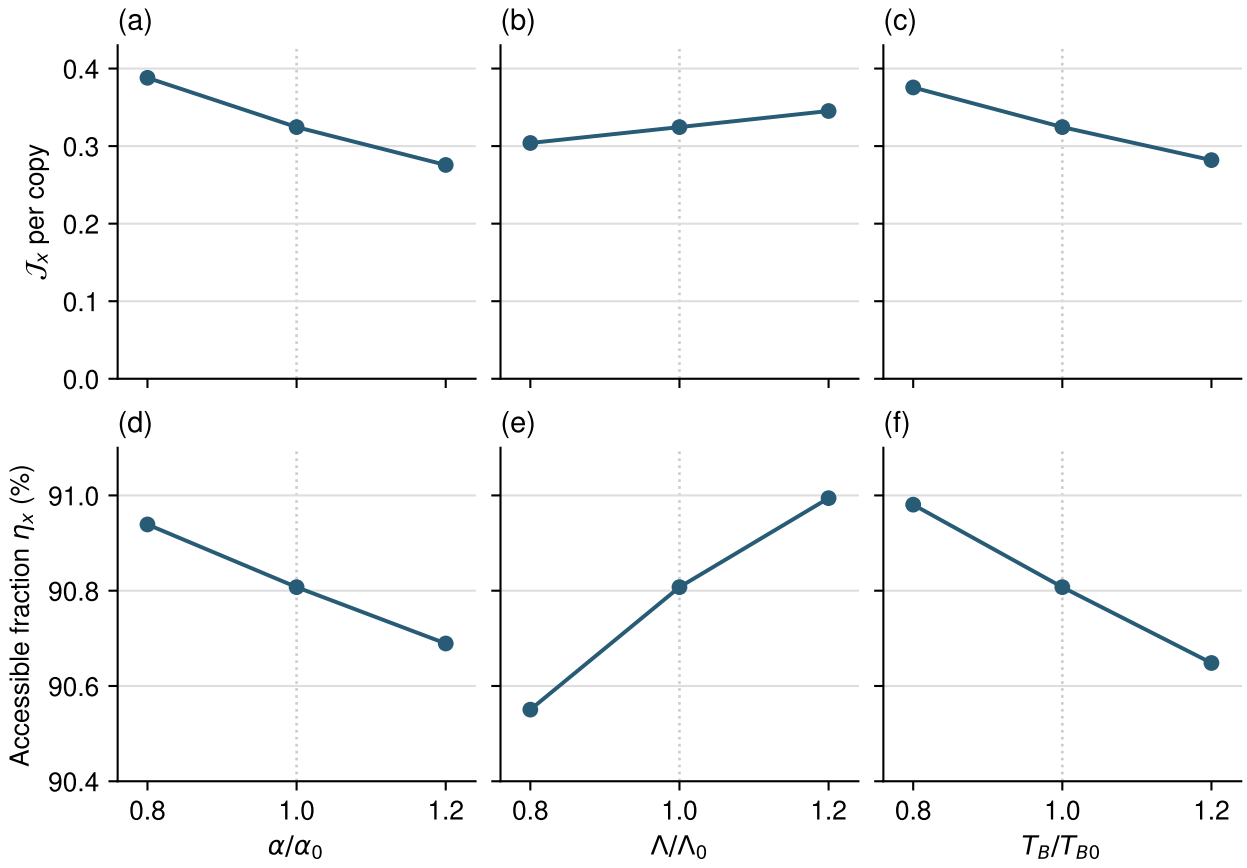

Fig. 3 Separate ±20% bath-parameter changes at Ω_c, with unchanged preparation and laboratory-x readout. Panels (a)–(c): absolute classical information. Panels (d)–(f): accessible fraction on an enlarged vertical scale. The columns vary α, Λ, and T_B, respectively; each horizontal axis is divided by its reference value. Lines only join the three computed values and do not certify intermediate points

3.5 Dependence on the known input direction

The reference advantage extends beyond the prescribed input. At the three original comparison amplitudes, both the mean QFI and laboratory-x information remain higher at the reference throughout a full 15° cone around $\boldsymbol{v}_0$, within the reconstructed numerical maps. A quadratic-form lower bound establishes this statement for every direction in the cone on those maps; it is not a statistical confidence region. Near-optimality of laboratory-x within the constant-axis class is checked at eight predefined tilts, but is not certified throughout the cone.

The known input $\boldsymbol{e}_y = (0, 1, 0)$ gives the opposite result. Its reference mean QFI is 0.025156, below both controls, and laboratory-x accesses only 0.5072% of that information. Another constant axis yields $\mathcal{J}_{\mathrm{num}} = 0.0136467$. Reduced retention and poor laboratory-x accessibility are therefore distinct effects, and neither advantage is uniform over inputs.

The operator structure singles out the x direction: both the periodic drive and the bath coupling act along x in Eq. (1), while the static splitting is along z. Alignment with the drive and coupling does not make σ_x conserved, because the static term does not commute with it. The observed input dependence is therefore quantified by the full dissipative map and its projection onto the fixed readout.

To compare known directions, we reconstruct the affine qubit map $\boldsymbol{r}_\theta = \boldsymbol{b} + \theta M \boldsymbol{v}$ from the six basis-state inputs $(I \pm \sigma_i)/2$, $i = x, y, z$. Each starts from the same factorized thermal bath.

The averaged information takes the quadratic form

$$\mathcal{J}_x(\boldsymbol{v}) = \boldsymbol{v}^{\mathsf{T}} A_x \boldsymbol{v}, \qquad \overline{F_Q}(\boldsymbol{v}) = \boldsymbol{v}^{\mathsf{T}} Q \boldsymbol{v}. \tag{18}$$

The SI defines these matrices and derives the cone bound. A separately propagated input checks the reconstruction. Laboratory-x remains unchanged; diagnostic constant-axis optimizations are performed separately for each known input and amplitude.

The SI also reports 13 named inputs, a deterministic hemisphere grid and all refinement tests. The grid gives descriptive counts, not preparation probabilities. Each encoding direction is assumed known; unknown preparation is not treated as a nuisance parameter.

3.6 Broader drive-amplitude scan

The three-point comparison establishes an advantage under a spectral selection made before the control propagations. The broader scan asks how exceptional and how narrow the reference performance is within a larger amplitude interval. It keeps the bath, phase, horizon and two known inputs $\boldsymbol{v}_0$ and $\boldsymbol{e}_y$ fixed while sampling $6 \leq \Omega \leq 12$, with a separate undriven comparison.

For $\boldsymbol{v}_0$, the largest sampled $\mathcal{J}_x = 0.324567$ occurs at $\Omega = 9.008106$, only 0.0202% above the original reference. For $\boldsymbol{e}_y$, the maximum instead occurs at $\Omega = 6.606250$. Figure 4 shows the contrasting undriven comparisons: the best sampled laboratory-x information for $\boldsymbol{v}_0$ is about twelve times its undriven value, whereas the undriven y input exceeds every sampled driven point in both laboratory-x information and mean QFI.

The main interval contains 112 evaluated amplitudes for both inputs. A frozen adaptive rule refines selected extrema and retains the old reference and controls. Two additional spectral minima were added as explicitly post-plan anchors, selected from the isolated spectrum before their HEOM propagation. Their values for $\boldsymbol{v}_0$ are lower than the sampled maximum near the original reference. The SI records the full selection rule, coordinates and checks; the finite-grid maxima do not certify continuous global optima.

A performance width describes the connected region around a sampled peak where $I(\Omega) \geq 0.9 I_{\mathrm{peak}}$. For laboratory-$x$ information, the interpolated widths are 0.07608 for $\boldsymbol{v}_0$ and 0.73158 for $\boldsymbol{e}_y$. These estimates use refined threshold brackets and assume one crossing inside each bracket. They are neither confidence intervals nor certified continuum error bounds. The SI gives the brackets, QFI widths and threshold-freezing rule. Drive energy is not held fixed across this comparison.

3.7 Numerical checks

Separate hierarchy-depth, bath-expansion and integrator refinements change the primary mean information quantities by at most 2.40×10^{-6} relatively across the tested points and five observation windows. A joint hierarchy and bath-expansion refinement at the reference also passes the predefined criteria. The input and amplitude studies meet their separate refinement criteria. The SI records the settings, initially failed diagnostics and their resolutions.

Independent evaluations of QFI and projective information agree with the Bloch formulas. Trace, Hermiticity, physicality and output-grid quadrature are also checked. All dynamical studies use the same HEOM implementation: these results support numerical stability at the reported settings, without providing independent second-code validation or rigorous continuum error bounds.

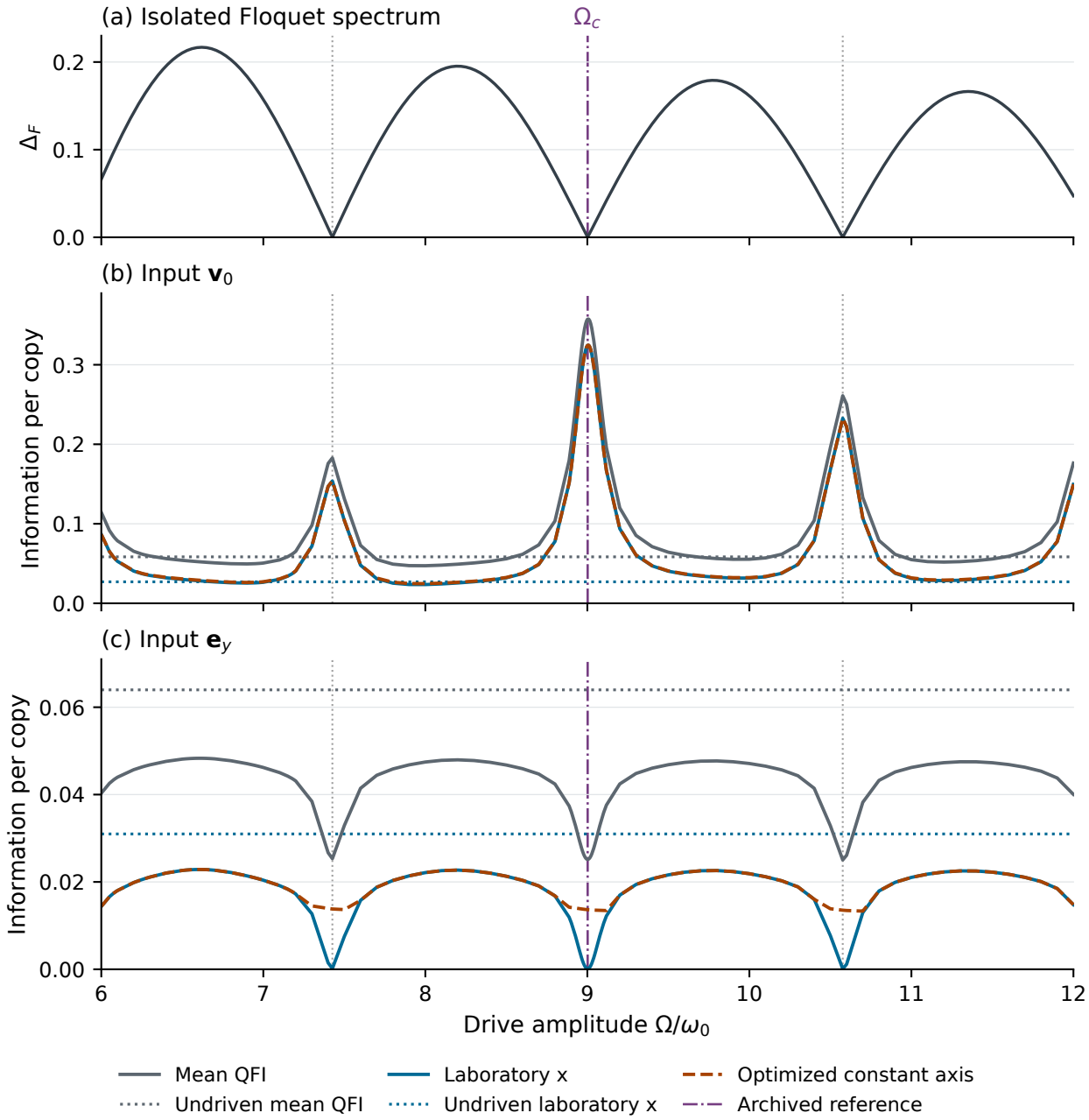

Fig. 4 Broader amplitude comparison at $T = 150$. (a) Reduced closed-system quasienergy gap. (b), (c) Mean QFI, laboratory-x information and numerically optimized constant-axis information for $\boldsymbol{v}_0$ and $\boldsymbol{e}_y$, respectively. The purple dash-dotted line marks the unchanged archived reference; gray vertical dotted lines mark the two additional spectral minima. Labeled horizontal dotted lines show the undriven mean QFI (gray) and laboratory-x information (blue), measured at $\Omega = 0$. Curves connect calculated points on an uneven adaptive grid; the two information panels use different vertical scales

4 Scope and interpretation

Operating point and causality. The reference-versus-control result supports an operating-point advantage for the specified delayed-readout experiment. It connects the established long-lived contrast near a crossing [6] to the information obtainable with a simple constant measurement. It does not isolate the quasienergy gap as the sole causal variable: changing Ω also changes Floquet modes, micromotion, and their effective coupling to the bath. The

broader scan locates sampled maxima and resolution-limited widths. Its adaptive design refines selected extrema and does not exclude narrower unresolved structures elsewhere.

Encoding and delayed access. The input is already strongly aligned with laboratory-x. At $t = 0$, $F_Q(0) = 1$ and $j_x(0) = v_x^2 = 0.8919622625$. Parameter-independent dynamics cannot increase the QFI above its initial value. The present comparison concerns how much information remains accessible after a prescribed distribution of delays, not an advantage over immediate readout or storage of an arbitrary unknown qubit.

Retained information and memory. A high fraction alone would be insufficient evidence for a Floquet or memory advantage. For example, Markovian dephasing generated by $\dot{\rho} = (\gamma/2)(\sigma_x\rho\sigma_x - \rho)$, with the same input, keeps $\mathcal{J}_x = v_x^2$ while its accessible fraction tends to one at long times. This analytical counterexample is derived in the Supplementary Information. It motivates the absolute-information controls used here. An advantage specifically due to non-Markovianity would additionally require a matched Markovian reference.

Measurement resources. The primary measurement class consists of ideal, terminal, binary Pauli projections with one time-independent laboratory axis. An illustrative postprocessing check in the SI adds a known, independent, symmetric outcome-flip probability of 1% or 5%. It reduces the absolute information while leaving the reference-to-control factors nearly unchanged. This check is conditional on that detector model. Losses, finite measurement duration, axis and drive-phase jitter, and the cost of a terminal basis rotation remain unmodelled. Consequently, no experimental superiority over engineered cavity or fluorescence readout is inferred. Known control and bath parameters are part of the statistical model; uncertainty in those quantities would require a separate multiparameter analysis.

5 Conclusion

For the prescribed input direction in this driven spin–boson benchmark, a constant laboratory-x projection provides nearly optimal information about the initial-state coefficient within the class of constant binary Pauli projections. The crossing reference retains more mean QFI and supplies about twice the readable information of two spectrum-selected controls. Direct axis optimization and an algebraic envelope separate constant-axis performance from the time-adaptive quantum reference. Separate bath variations retain a high accessible fraction while changing the absolute information.

The input study establishes a full 15° neighborhood with a reference advantage in the numerical maps, while the known y input reverses the comparison. The broader amplitude scan places the original reference close to its largest sampled information and quantifies a narrow performance width. For the y input, even the best sampled driven information is below its undriven value. The comparisons do not isolate the quasienergy gap as the cause, or establish protection of an arbitrary unknown qubit, a continuous global optimum, or a specifically non-Markovian advantage. Within this scope, they provide a reproducible benchmark for evaluating information retention and fixed-axis accessibility together.

Acknowledgements

The author is grateful for valuable discussions with the late Stig Stenholm.

Statements and declarations

Funding. No external funding was received.

Competing interests. The author declares no competing interests.

Author contributions. Matthias Jakob is the sole author and is responsible for the research design, analysis, interpretation, and final manuscript.

Data and code availability. All data supporting this study, including frozen configurations, endpoint Bloch trajectories, available solver logs, analysis and figure code, and reproduction instructions, are included in Online Resource 2 (`ESM2.zip`). The primary batches, input-direction study and broader amplitude scan are supplied in full, including initial failed diagnostics and their resolutions. Online Resource 1 (`ESM1.pdf`) documents the methods and numerical checks. The corresponding public Zenodo data and code record is available at `https://doi.org/10.5281/zenodo.24026283` [30]. The journal version of Online Resource 1 adds bibliographic references to the archived methods document; its equations and numerical results are unchanged. Online Resource 2 is byte-identical to the archived data package. The manuscript source archive also supplies `render_fig4.py`, which reproduces the display-only revision of Fig. 4 from unchanged archived results.

Use of AI tools. OpenAI Codex assisted with code development, numerical verification workflows, literature organization, and substantive manuscript drafting and revision, including the present revision in November 2026. The author directed this use and retains responsibility for checking the scientific statements, references, numerical results, and final text.

Ethics, Consent to Participate, and Consent to Publish declarations: not applicable. This theoretical and computational study involves no human participants, animals, or personal data.

Author identifier. ORCID: `https://orcid.org/0009-0004-0798-3289`.

Supplementary Information

Online Resource 1 (`ESM1.pdf`). Model conventions, primary operating points, affine-map input analysis, cone bounds, amplitude refinement and width brackets, convergence checks, and reproduction instructions.

Online Resource 2 (`ESM2.zip`). Endpoint trajectories and metadata for 315 antipodal records (630 endpoint propagations), frozen study plans, available run logs, axis optimization, analysis and figure code, and checksums.

References

[1] J. H. Shirley. Solution of the Schrödinger equation with a Hamiltonian periodic in time. *Physical Review*, 138:B979–B987, 1965. `https://doi.org/10.1103/PhysRev.138.B979`.

[2] Hideo Sambe. Steady states and quasienergies of a quantum-mechanical system in an oscillating field. *Physical Review A*, 7:2203–2213, 1973. `https://doi.org/10.1103/PhysRevA.7.2203`.

[3] Milena Grifoni and Peter Hänggi. Driven quantum tunneling. *Physics Reports*, 304(5–6): 229–354, 1998. `https://doi.org/10.1016/S0370-1573(98)00022-2`.

[4] Takashi Mori. Floquet States in Open Quantum Systems. *Annual Review of Condensed Matter Physics*, 14:35–56, 2023. https://doi.org/10.1146/annurev-conmatphys-040721-015537.

[5] Pranav S. Mundada, András Gyenis, Ziwen Huang, Jens Koch, and Andrew A. Houck. Floquet-Engineered Enhancement of Coherence Times in a Driven Fluxonium Qubit. *Physical Review Applied*, 14:054033, 2020. https://doi.org/10.1103/PhysRevApplied.14.054033.

[6] Pietro Marco Follia, Bassano Vacchini, and Heinz-Peter Breuer. Control of memory effects in a spin-boson system by periodic driving. *Physical Review A*, 113:022203, 2026. https://doi.org/10.1103/g55y-8j7x.

[7] Pietro Follia, Heinz-Peter Breuer, and Bassano Vacchini. Floquet time-convolutionless master equation for non-Markovian driven quantum systems, 2026. URL https://doi.org/10.48550/arXiv.2607.24406. Preprint, arXiv:2607.24406.

[8] Ziwen Huang, Pranav S. Mundada, András Gyenis, David I. Schuster, Andrew A. Houck, and Jens Koch. Engineering Dynamical Sweet Spots to Protect Qubits from 1/f Noise. *Physical Review Applied*, 15:034065, 2021. https://doi.org/10.1103/PhysRevApplied.15.034065.

[9] Anthony Gandon, Camille Le Calonnec, Ross Shillito, Alexandru Petrescu, and Alexandre Blais. Engineering, Control, and Longitudinal Readout of Floquet Qubits. *Physical Review Applied*, 17:064006, 2022. https://doi.org/10.1103/PhysRevApplied.17.064006.

[10] Zhaoyou Wang and Amir H. Safavi-Naeini. Quantum control and noise protection of a Floquet 0–π qubit. *Physical Review A*, 109:042607, 2024. https://doi.org/10.1103/PhysRevA.109.042607.

[11] Samuel L. Braunstein and Carlton M. Caves. Statistical distance and the geometry of quantum states. *Physical Review Letters*, 72:3439–3443, 1994. https://doi.org/10.1103/PhysRevLett.72.3439.

[12] Matteo G. A. Paris. Quantum estimation for quantum technology. *International Journal of Quantum Information*, 7(supp01):125–137, 2009. https://doi.org/10.1142/S0219749909004839.

[13] O. E. Barndorff-Nielsen and R. D. Gill. Fisher information in quantum statistics. *Journal of Physics A: Mathematical and General*, 33:4481–4490, 2000. https://doi.org/10.1088/0305-4470/33/24/306.

[14] Xiao-Ming Lu, Shunlong Luo, and C. H. Oh. Hierarchy of measurement-induced Fisher information for composite states. *Physical Review A*, 86:022342, 2012. https://doi.org/10.1103/PhysRevA.86.022342.

[15] Wei Zhong, Zhe Sun, Jian Ma, Xiaoguang Wang, and Franco Nori. Fisher information under decoherence in Bloch representation. *Physical Review A*, 87:022337, 2013. https://doi.org/10.1103/PhysRevA.87.022337.

[16] Heinz-Peter Breuer, Elsi-Mari Laine, and Jyrki Piilo. Measure for the Degree of Non-Markovian Behavior of Quantum Processes in Open Systems. *Physical Review Letters*, 103:210401, 2009. https://doi.org/10.1103/PhysRevLett.103.210401.

[17] Xiao-Ming Lu, Xiaoguang Wang, and C. P. Sun. Quantum Fisher information flow and non-Markovian processes of open systems. *Physical Review A*, 82:042103, 2010. https://doi.org/10.1103/PhysRevA.82.042103.

[18] Utkarsh Mishra and Abolfazl Bayat. Integrable quantum many-body sensors for AC field sensing. *Scientific Reports*, 12:14760, 2022. https://doi.org/10.1038/s41598-022-17381-y.

[19] Si-Yuan Bai and Jun-Hong An. Floquet Engineering to Overcome No-Go Theorem of Noisy Quantum Metrology. *Physical Review Letters*, 131:050801, 2023. https://doi.org/10.1103/PhysRevLett.131.050801.

[20] Asghar Ullah, Hasan Mermer, Melih Özkurt, Igor Lesanovsky, and Özgür E. Müstecaplıoğlu. Harnessing Floquet dynamics for selective metrology in few-qubit systems. *Physical Review B*, 113:075123, 2026. https://doi.org/10.1103/l9ms-79hn.

[21] M. A. Manya, Andrei Tsypilnikov, and Fernando Iemini. Optimal observables for quantum-enhanced sensing and applications in a Floquet time crystal sensor, 2026. URL https://doi.org/10.48550/arXiv.2606.26248. Preprint, arXiv:2606.26248.

[22] Yoshitaka Tanimura. Numerically "exact" approach to open quantum dynamics: The hierarchical equations of motion (HEOM). *The Journal of Chemical Physics*, 153:020901, 2020. https://doi.org/10.1063/5.0011599.

[23] Heinz-Peter Breuer and Francesco Petruccione. *The Theory of Open Quantum Systems*. Oxford University Press, Oxford, 2007. https://doi.org/10.1093/acprof:oso/9780199213900.001.0001.

[24] Neill Lambert, Tarun Raheja, Simon Cross, Paul Menczel, Shahnawaz Ahmed, Alexander Pitchford, Daniel Burgarth, and Franco Nori. QuTiP-BoFiN: A bosonic and fermionic numerical hierarchical-equations-of-motion library with applications in light-harvesting, quantum control, and single-molecule electronics. *Physical Review Research*, 5:013181, 2023. https://doi.org/10.1103/PhysRevResearch.5.013181.

[25] N. Lambert, E. Giguère, P. Menczel, B. Li, P. Hopf, G. Suárez, M. Gali, J. Lishman, R. Gadhvi, R. Agarwal, A. Galicia, N. Shammah, P. Nation, J. R. Johansson, S. Ahmed, S. Cross, A. Pitchford, and F. Nori. QuTiP 5: The quantum toolbox in Python. *Physics Reports*, 1153:1–62, 2026. https://doi.org/10.1016/j.physrep.2025.10.001.

[26] Sigmund Kohler and Jesús Casado-Pascual. Hidden time-nonlocal Floquet symmetries. *Quantum*, 10:2112, 2026. https://doi.org/10.22331/q-2026-05-21-2112.

[27] Dieter Kraft. A software package for sequential quadratic programming. Technical Report DFVLR-FB 88-28, DFVLR, 1988.

[28] Rainer Storn and Kenneth Price. Differential evolution—a simple and efficient heuristic for global optimization over continuous spaces. *Journal of Global Optimization*, 11(4): 341–359, 1997. https://doi.org/10.1023/A:1008202821328.

[29] Pauli Virtanen, Ralf Gommers, Travis E. Oliphant, Matt Haberland, Tyler Reddy, David Cournapeau, Evgeni Burovski, Pearu Peterson, Warren Weckesser, Jonathan Bright, Stéfan J. van der Walt, Matthew Brett, Joshua Wilson, K. Jarrod Millman, Nikolay Mayorov, Andrew R. J. Nelson, Eric Jones, Robert Kern, Eric Larson, C J Carey, İlhan Polat, Yu Feng, Eric W. Moore, Jake VanderPlas, Denis Laxalde, Josef Perktold, Robert Cimrman, Ian Henriksen, E. A. Quintero, Charles R. Harris, Anne M. Archibald, Antônio H. Ribeiro, Fabian Pedregosa, Paul van Mulbregt, and SciPy 1.0 Contributors. SciPy 1.0: Fundamental algorithms for scientific computing in Python. *Nature Methods*, 17(3):261–272, 2020. https://doi.org/10.1038/s41592-019-0686-2.

[30] Matthias Jakob. Data and code for "Fixed laboratory-axis readout of retained qubit information near a Floquet crossing". Zenodo, 2026. URL https://doi.org/10.5281/zenodo.24026283. Version 2.0.1; data and code.

Supplementary Files

This is a list of supplementary files associated with this preprint. Click to download.

- ESM1.pdf
- ESM2.zip